Influence of Nb alloying on Nb recrystallization and the upper critical field of Nb$_3$Sn

Nawaraj Paudel ⬤, Chiara Tarantini ⬤, Shreyas Balachandran ⬤,* William L. Starch, Peter J. Lee ⬤, and David C. Larbalestier ⬤†
Applied Superconductivity Center, National High Magnetic Laboratory, Florida State University, Tallahassee, Florida 32310, USA

Nb$_3$Sn conductors are important candidates for high-field magnets for particle accelerators, and they continue to be widely used for many laboratory and nuclear magnetic resonance magnets. However, the critical current density, J_c, of present Nb$_3$Sn conductors declines swiftly above 12–15 T. State-of-the-art Ta- and Ti-doped strands exhibit upper critical field, H_{c2}, values of ∼24–26.5 T (4.2 K) and do not reach the Future Circular Collider target J_c, which serves as the present stretch target for Nb$_3$Sn development. As recently demonstrated, to meet this goal requires enhanced vortex pinning but an independent and supplementary approach is to significantly enhance H_{c2}. In this study, we have arc melted multiple Nb alloys with added Hf, Zr, Ta, and Ti and drawn them successfully into monofilament wires to investigate the possibilities of H_{c2} enhancement through alloying. $H_{c2}(T)$ was measured for all samples in fields up to 16 T and some up to 31 T. We have found that all alloys show good agreement with the standard Werthamer, Helfand, and Hohenberg fitting procedure without the need to adjust the paramagnetic limitation parameter (α) and spin-orbit scattering parameter (λ_{so}). The evaluation of dH_{c2}/dT near T_c, which is proportional to the electronic specific heat coefficient γ and the normal state resistivity ρ_n, allows a better understanding of the induced disorder introduced by alloying in the A15 phase. So far, we have observed that Hf alloying of pure Nb can enhance $H_{c2}(0)$ by 3–4 T to ∼28 T, while adding just 1 at. % Hf or Zr into a Nb-4 at. % Ta base alloy can raise $H_{c2}(0)$ to ∼31 T. Very importantly we find that Hf and Zr raise the alloy recrystallization temperature above the usual A15 reaction temperature range of 650 °C−750 °C, thus ensuring denser A15 phase nucleation in the Nb alloy grain boundaries, possibly leading to a more homogeneous A15 phase Sn content and refined A15 grain size. The potential for further advancements in Nb$_3$Sn properties is explored in relation to the recrystallization of the Nb alloy and the factors controlling the upper critical field.

I. INTRODUCTION

At present, most large superconducting magnet applications like the Large Hadron Collider (LHC) at CERN and magnetic resonance imaging systems use Nb-Ti, whose practical field limit is about 12 T. Another low temperature superconductor, long used for higher field laboratory solenoid magnets, is Nb$_3$Sn. It is now being applied to accelerator dipoles, but such magnets demand the highest possible current density because their magnetic efficiency is approximately half that of solenoid magnets [1], a real challenge now that future accelerator goals for dipole magnets are well beyond 10 T (12–16 T). A recent four-layer Nb$_3$Sn dipole magnet achieved 14 T [2] but getting to a 16 T dipole is quite impossible even with the latest generation of internal-tin RRP (rod re-stacked process) wires manufactured by Bruker Energy & Supercon-Technologies Inc. [3]. NMR requires solenoid magnets up to 23 T that require sub–2 K operation for maximum field. Significant efforts have been made to optimize the non-Cu critical current density (J_c) which is a key parameter for such Nb$_3$Sn applications [4–6], reaching J_c (4.2 K, 16 T) values up to ∼1375 A/mm^2, still below the Future Circular Collider (FCC) target J_c of 1500 A/mm^2 (4.2 K, 16 T). In Nb$_3$Sn conductors, there exists a continuous trade-off between maximizing the upper critical field (H_{c2}) and vortex pinning, which decides the critical current density (J_c) [7]. In Nb$_3$Sn conductors, the reaction temperature increase results in larger grain sizes that lower vortex pinning and current density (J_c) [8], but it does increase H_{c2}, reduce the transition breadth, and raise the irreversibility field H_{irr} [9], which is beneficial for practical applications. To utilize Nb$_3$Sn in the HiLumi LHC upgrade, striking a good balance between maximizing the upper critical field and maximizing vortex pinning was necessary. To attain the best J_c (16 T) for the FCC will require a multifaceted improvement that will include maximizing H_{c2}, compositional uniformity, and enhancing grain-boundary pinning and/or "artificial pinning" (i.e., by oxide particles). Independently, the highest possible conversion to A15 phase formation from the so-called non-Cu package is needed too: the Nb alloy, the Sn source, any oxygen source for artificial pinning centers, and the diffusion barrier needed to protect the residual resistance ratio of the stabilizing and protective copper of the conductor [6,7] must be optimized so that the highest possible cross-sectional fraction of high J_c A15 is formed. In short, the further development of Nb$_3$Sn conductor technology is a complex optimization of often conflicting variables.

An underlying component of achieving the FCC goal is by maximizing H_{c2}. Orlando *et al.* observed that moderately increasing ρ_n in Sn-deficient, binary Nb-Sn films raised

---

*Present address: Jefferson Laboratory, Newport News, Virginia 23606, USA.
†Contact author: larbalestier@asc.magnet.fsu.edu

$H_{c2}(0)$ to ~ 30 T, while also degrading T_c to below 17 K, in strong contrast to $H_{c2}(0) \sim 21$ T for clean-limit, stoichiometric Nb$_3$Sn. Their study showed that "dirty," i.e., disordered, samples could possess higher H_{c2} even though they are off-stoichiometric [10]. The inevitability of some Sn (and thus superconducting property) gradients in the A15 Nb$_3$Sn layer of present conductors results from a Sn activity drop as the reaction nears completion. To optimize the amount of A15 in the non-Cu package the diffusion reaction of Sn into Nb alloy to form doped Nb$_3$Sn effectively becomes an exhaustion reaction with low-Sn A15 compositions developing at the A15 reaction front during later stages of the reaction. An extensive study of these trade-offs for many reactions of binary and Nb-4 at. % Ta high-tin powder-in-tube (PIT) conductor was published by Godeke *et al.* and Fischer [9,11], which showed the way in which the compositional gradients produced by restricted reactions causes a marked lowering of the irreversibility field (H_{irr}; defined by the bottom of the resistive field transition) without much affecting the top of the superconducting transition which defines H_{c2} [9]. This transition breadth is tied to the Sn gradient across the A15 layer. Earlier experiments showed that H_{c2} (0) varied almost linearly ~ 5 T per at. % between 19.5 and 24 at. % Sn while the critical transition temperature T_c [12] also exhibited a linear dependence throughout the A15 phase (from 6 K at 18 at. % Sn to 18 K at stoichiometry) [13]. Beyond 24 at. % Sn, T_c and H_{c2} no longer follow a linear composition dependence due to the cubic-tetragonal phase transformation of the A15 lattice (lattice softening produces a lower phonon frequency) [14]. The presently used Ta- and Ti-doped high J_c Nb$_3$Sn conductors have T_c, H_{c2} values that appear to show a linear dependence on at.% Sn over the whole composition range [15] because the dopants suppress the martensitic transformation, shorten the electron mean free path, and raise H_{c2}. To better understand these alloying effects, Suenaga [16] doped Nb with Ta, Ti, Hf, and Zr and demonstrated that H_{c2} was raised by ~ 3 T for additions of 4 at. % Ta and 0.8 at. % Ti. The alloying dependence of the residual resistivity shows that Ti is at least twice as effective as an A15 disordering agent as Ta [16], the increase in H_{c2} correlating well to increased normal state resistivity. In contrast to Ti and Ta, Zr by itself lowered T_c [17]. Later, both Ta and Ti emerged into PIT and RRP wire technology and Ti doping by insertion of occasional Nb47Ti filaments into RRP conductors, which then became the standard method of doping RRP conductors. Heald *et al.* and Tarantini *et al.* made an extended x-ray absorption fine structure (EXAFS) study on Ta, Ti, Ta+Ti RRP standard wires and showed that Ta substitutes on both Nb and Sn sites, whereas Ti substitutes only on Nb sites [18,19]. The implication is that Ti, sitting only on Nb A15 lattice sites, is a more effective disordering agent than Ta sitting on both Sn and Nb sites. Commercially, Ta, Ti, and combined Ta+Ti dopants have been explored to improve the upper critical field H_{c2}, but a complication is that even the best state-of-the-art modern conductors show compositional gradients across the A15 layer that cause a separation between the onset of dissipation at the irreversibility field H_{irr} (where J_c becomes zero) and the full restoration of the normal state at H_{c2} [15]. Longer and higher temperatures, thus more complete, reactions move H_{irr} closer to H_{c2}, which tends to be more insensitive to A15 reaction conditions [9]. We must

therefore be concerned more about H_{irr} than H_{c2} for conductor optimization [9,19]. Complications due to strain either due to the tetragonal phase transition or operational stresses are considered to be second-order effects when the conductor architecture is kept constant, and minimization of strain is practiced as is the case in all the experiments reported here.

Time of reaction may be of interest, too, for magnet builders, and various studies have shown that different alloying element additions have effects on the A15 reaction rates, with Ti, for example, producing faster reaction than Ta additions [20,21]. It has also been observed that Zn, Al, or Mg additions increase the rate of Nb$_3$Sn formation, even if they do not dissolve into the Nb$_3$Sn layer [22]. However, Ta, Hf, and Ga do dissolve into the A15 layer and thus can influence the intrinsic superconducting properties [17,22–25]. For instance, Ga and Hf additions to Nb$_3$Sn have been reported to improve J_c(16 T) by one order of magnitude, T_c by 1 K, and upper critical field by 5 T with respect to binary Nb$_3$Sn [26–28], though few studies showed good quality high-field H_{c2} transitions, making it uncertain for a long time whether studies of new alloys were justified or not. Only with the issuance of the FCC specification has the issue become so important that the optimum alloying of Nb$_3$Sn deserves revisiting [29–32]. The precursor to this study was recent work made at the Applied Superconductivity Center and by some other groups which shows that the addition of group IV (Hf, Zr) elements to Nb-4 at. % Ta enhances H_{irr}, although the addition of O$_2$ might slightly degrade it [29,30,32,33]. The best present state-of-the-art Ta- and Ti-doped RRP conductors show H_{c2}(4.2 K) values in the range $24 - 26.5$ T. But, as noted above, the overall goal must always be to develop a high-field conductor with the finest possible A15 grain size and minimum H_{irr}-H_{c2} transition breadth. To this end, this paper focuses on the following issues:

(1) Developing a thorough understanding of how the upper critical field of Nb$_3$Sn evolves as it is doped with elements such as Ta, Hf, Zr, Ti, and Ga that enter the A15 phase. We used our arc melter to make Nb alloys of many compositions and then reacted them by diffusion reaction with Cu-Sn and Cu-Ga-Sn mixtures.

(2) Sekine *et al.* reported that additions of Hf, and Ga and Hf together significantly enhanced the H_{c2} of Nb$_3$Sn conductors [27]. Accordingly, we restudied the effect of adding Hf to Nb (with Ga added to the Cu-Sn mixture), but also investigated the Hf-Ga effectiveness when combined with the NbTa alloy, which by itself leads to a higher Nb$_3$Sn H_{c2} with respect to the use of pure Nb. This more complex alloy (NbTaHf) is in fact a candidate for the realization of new high-field conductors.

(3) With present Ti and Ta-doped Nb, $H_{c2}(0)$ can be increased from 25 to 27 T to less than 30 T [9,15,18]. Because these enhancements are relatively small, we made careful measurements of $H_{c2}(T)$ for all our alloys and investigated whether the H_{c2} enhancement requires consideration of paramagnetic limiting or spin-orbit scattering effects, finding that they do not. We show that our optimum addition of both Ta and Hf increases $H_{c2}(0)$ to over 30 T.

(4) Because A15 grain refinement is critical to enhancing vortex pinning, we studied the effect of alloying on the stability of the cold-worked alloy grain structures, finding that

both Zr and Hf are effective in inhibiting the recovery and recrystallization of the Nb alloy to above the normal A15 reaction temperature range [30,32,33].

II. EXPERIMENTAL METHODS

We arc melted custom alloys by using commercial NbxTa ($x = 0, 2, 4$ at. %) base alloys and adding Hf, Zr, and Ti by themselves or in combination. All Nb alloys are referred to by the commonly used notation specifying the atomic percentage of their dopant(s) (e.g., Nb2Ta2Hf is the alloy made with 96 at. % Nb, 2 at. % Ta, and 2 at. % Hf) unless otherwise specified. Our in-house, arc melter was used to produce batches of ∼35 g ingots. Loss of material during the melting process was negligible (<0.2 g).

Vickers hardness tests, superconducting quantum interference device (SQUID) magnetometer characterizations, and scanning electron microscopy (SEM) analyses were conducted on the as-cast Nb alloys to evaluate their quality before they were drawn into wires. All alloys had a high T_c onset ($\geqslant 9$ K) and sharp transitions ($\leqslant 0.25$ K). Our wire design, consisted in surrounding a Nb-alloy core rod with Cu + Sn(+Ga) powder, and then further cladding with a composite Ta/Cu tube as in [32], as depicted in Fig. 1. The central alloy rod was swaged from the irregular arc-melted billet to a 3-mm-diameter, 400-mm-long rod. The Cu-Sn powders used had an initial mesh size of 320 (∼50 μm) and were mixed in a 6:5 atomic ratio. The initial package was drawn to a final wire diameter of 2 mm. The total true strain (ε) is determined by the cross-sectional area reduction, $\varepsilon = \ln(A_0/A_f)$, where A_0 is the initial area, and A_f is the final area.

To determine the Vickers hardness of the as-cast alloy and its correlation with the true drawing strain, all arc-melted ingots were swaged using a 20% reduction in area and samples were taken every two to three passes. The Vickers hardness was measured on metallographically polished transverse sections using a 300 g load. The SQUID magnetometer measurements from 4.0 to 12.0 K were taken on the alloys showing transition widths of typically less than 0.3 K. The monofilament test beds were made with Cu + Sn and Cu + Sn + Ga powders. The starting composition of the Cu + Sn powder was Cu-45 at.% Sn (Cu_6Sn_5 equivalent), whereas the used Cu + Sn + Ga powder mixes were Cu-25 at. % Sn-20 at. % Ga and Cu-30 at. % Sn-2 at. % Ga. The monofilament test beds were drawn to a filament diameter of 2 mm followed by a two-step heat treatment. A 550 °C hold was previously chosen to decompose SnO_2 in wires containing it; however, it is also used in this paper for direct comparison to the results obtained earlier on Hf/Zr/Ta-doped samples using the same heat treatment schedule [32,34]. A second step ranging between 650 °C and 850 °C was used for the A15 reactions. Prior to transport measurements the external Cu was etched away, and the Ta tube cut open to extract the central alloyed-Nb rod surrounded by the A15 layer on which the contacts were made. Resistive transport characterizations to determine $H_{c2}(T)$ were performed in our 16 T Quantum Design physical property measurement system (PPMS) and some wires were measured up to 31 T at the National High Magnetic Field Laboratory (NHMFL). A Zeiss 1540 EsB field-emission scanning electron microscope (FESEM) was used to evaluate the
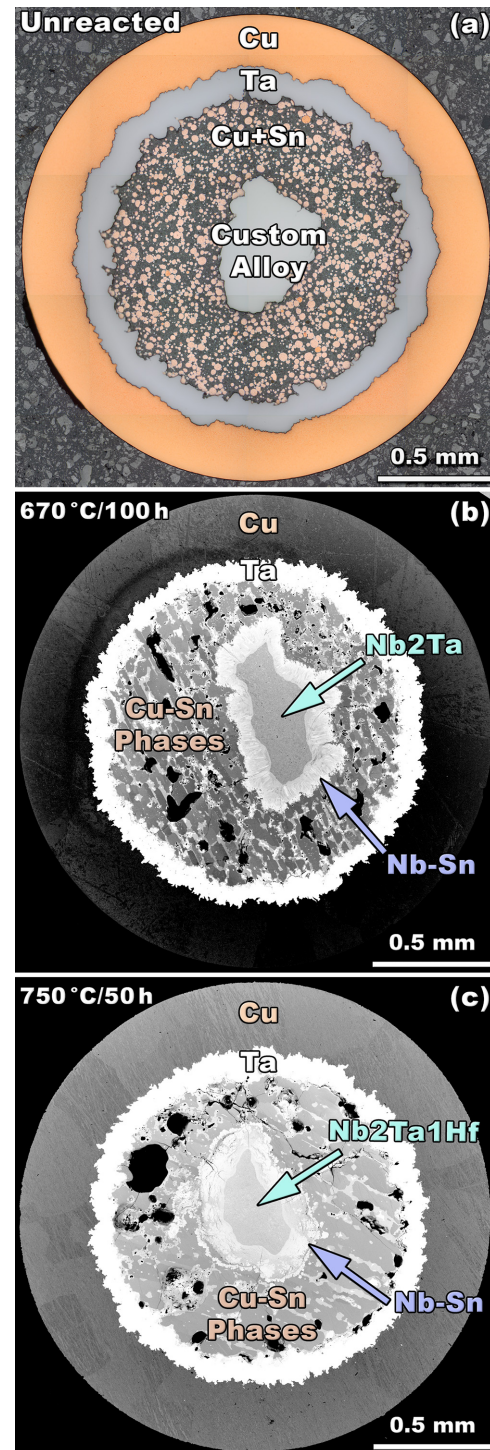
FIG. 1. (a) Light microscope image of a cross section of an unreacted monofilament wire. In-house melted custom alloy rods were placed in the center of a Cu + Sn powder mixture fitted inside a commercial seam welded Ta tube which was sheathed in a Cu tube. (b) and (c) Typical FESEM-BSE cross sections of reacted monofilament wires. The light contrast at the perimeter of the central alloy rods reveals the reacted layers.

microstructures on transverse wire cross sections prepared by metallographic polishing. The samples were imaged with a solid-state back-scattered electron (BSE) detector, and energy dispersive x-ray spectroscopy (EDXS) was used to study the
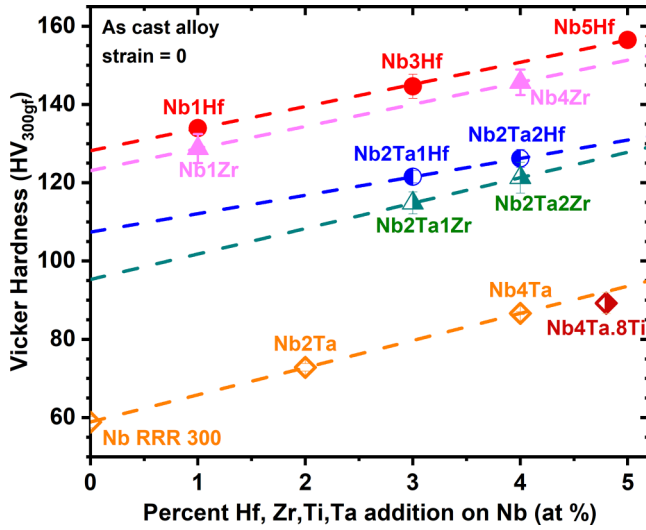
FIG. 2. Vickers hardness as a function of EDS-determined alloy compositions. The Vickers hardness increases in all cases as the dopant addition increases.

FIG. 3. Vicker hardness after 3 h anneals at the stated heat treatment (HT) temperatures used to study the recrystallization behavior of Nb4Ta and Nb4Hf. It is clear that Hf significantly delays recrystallization as compared to the equivalent Nb-Ta alloy.

elemental compositions of the as-cast alloys and their A15 layers. In the following we will identify the doped Nb_3Sn samples according to their atomic percentage doping content only (e.g., 4Ta1Hf is the doped Nb_3Sn wire made with the Nb4Ta1Hf alloy).

III. RESULTS

A. Recrystallization and microstructural characterizations

The Vickers hardness H_V was used to evaluate the potential wire fabricability and its response to heat treatment in the A15 reaction window. H_v versus alloy content and type is shown in Fig. 2. All alloys in both the as-cast and worked states were hardened by additions of Ta, Zr, and Hf. Consistent with their size difference, the larger Hf and Zr atoms hardened the Nb more strongly than Ta, but this did not make the alloys challenging to draw. The increase in hardness with increasing Hf, Zr, and Ta solute in the binary/ternary alloys is linear with the total percentage of addition in all cases. A comparison of the recrystallization behavior of Nb4Hf and Nb4Ta after 3 h anneals at different temperatures is presented in Fig. 3, which clearly shows that H_V starts to decline above about 400 °C for Nb4Ta but also that this is delayed to 650 °C−700 °C for the Nb4Hf alloy. The initial recovery processes occurring within the grains shown in Fig. 4 have little effect on grain size even up to 800 °C and real grain growth for the Nb4Hf alloy is only visible in the sample annealed at 1000 °C, which is consistent with the hardness change behavior shown in Fig. 3. We also see some high atomic number (light) precipitates in the recrystallized structure [Fig. 4(d)], which the SEM-EDXS analysis shows to be Hf rich; those are more evident after the high-temperature heat treatment. FESEM-BSE imaging revealed both the Nb_3Sn A15 layer and the partly annealed alloy structure in the unreacted cores in Fig. 5. The evident recrystallization of the Nb2Ta, Nb4Ta, Nb0.8Ti, and Nb4Ta0.8Ti alloy cores is highlighted by channelling contrast in the BSE images. In contrast, the Hf and Zr alloyed
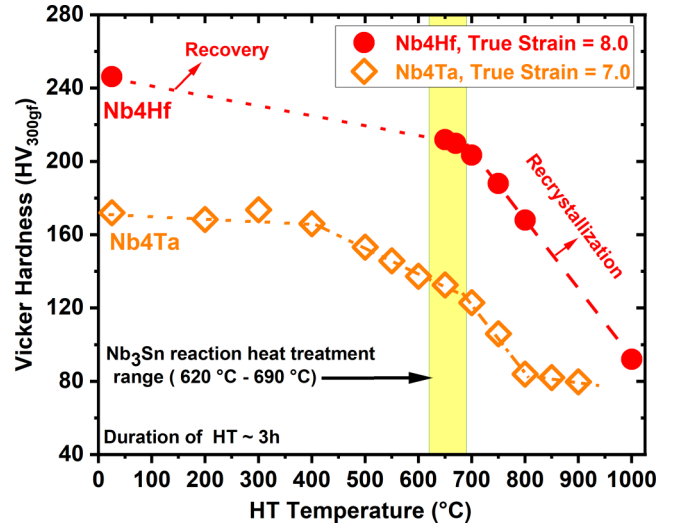
(Nb2Ta2Hf, Nb2Ta2Zr) core rods retain their worked structure, even after A15 reactions at 550 °C/50 h+750 °C/50 h.

B. $H_{c2}(T)$ and its analysis

Small current ($\sim$10 mA), resistive transport characterizations, $R(T,H)$, to determine $H_{c2}(T)$ were performed with contacts on the bare Nb_3Sn layers on all the reacted wires in the 16 T PPMS using temperature sweeps over the range 1.9– 22 K. Some wires were also measured in higher fields in the 31 T resistive magnet at the NHMFL using constant-temperature field sweeps in the range 0−31 T. Typical resistive transition traces using temperature sweeps at constant field are shown
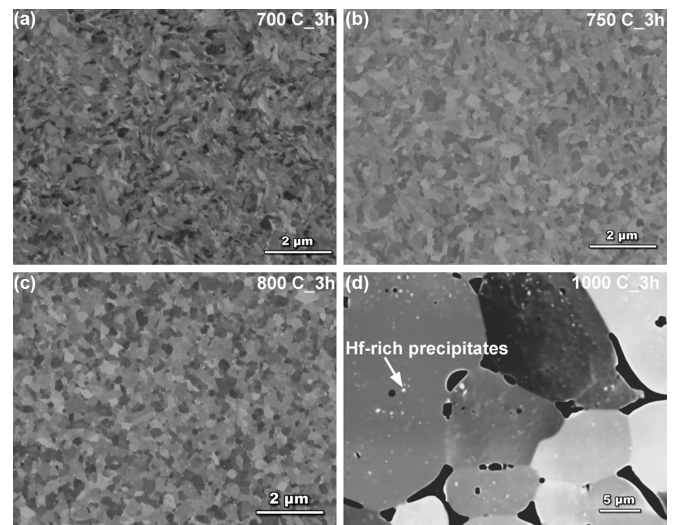
FIG. 4. Microstructural evolution of Nb4Hf from (a) 700 °C for 3 h, (b) 750 °C for 3 h, (c) 800 °C for 3 h, and (d) 1000 °C for 3 h (FESEM-BSE images). The annealing of Nb4Hf has little effect on grain size even up to 800 °C and grain growth is only visible at an annealing temperature of 1000 °C.
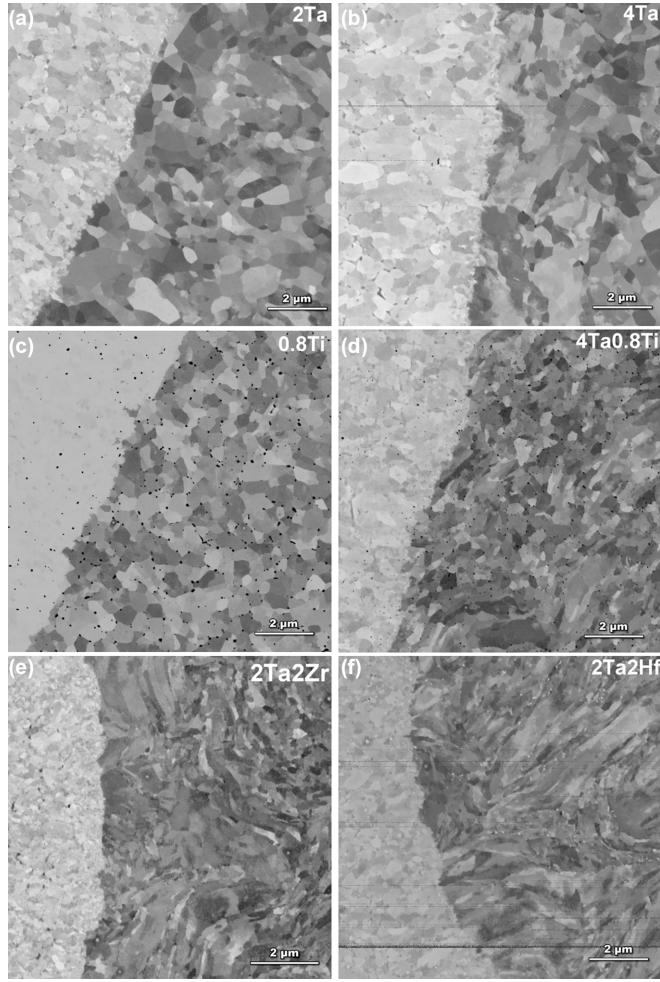
FIG. 5. Representative FESEM-BSE images of the Nb-alloy core/Nb_3Sn interface after the monofilaments were reacted at 550 °C/50 h+750 °C/50 h. The darker Nb-alloy cores are on the right and the lighter A15 diffusion layers are on the left of the interface (sample IDs are indicated in the top right corner of each image). Electron channeling contrast in the corresponding images reveals recrystallized microstructures in the unreacted NbxTa($x =$ 2, 4), Nb0.8Ti, and Nb4Ta0.8Ti alloys. In contrast, the Nb2Ta2Hf and Nb2Ta2Zr alloys retain a deformed, cold-worked grain structure.

in Fig. 6(a) for a 4Ta1Hf wire (the normal state magnetoresistance originates in the residual unreacted Nb alloy, not the A15 layer). $H_{c2}(T)$ was evaluated at 90% of the normal state resistance for both PPMS 16 and 31 T data sets (two pieces of the same wire were used). The data in Fig. 6(b) is fitted by the full Werthamer, Helfand, and Hohenberg (WHH) relation [35]:

$$\ln \frac{1}{t} = \left(\frac{1}{2} + \frac{i\lambda_{so}}{4\gamma} \right) \psi \left(\frac{1}{2} + \frac{\bar{h} + \frac{1}{2}\lambda_{so} + i\gamma}{2t} \right)$$

$$+ \left(\frac{1}{2} - \frac{i\lambda_{so}}{4\gamma} \right) \psi \left(\frac{1}{2} + \frac{\bar{h} + \frac{1}{2}\lambda_{so} - i\gamma}{2t} \right) - \psi \left(\frac{1}{2} \right)$$

(where $\gamma = [(\alpha\bar{h})^2 - (\frac{1}{2}\lambda_{so})^2]$, $t = \frac{T}{T_c}$, $\bar{h} = \frac{4H_{c2}(T)}{\pi^2 T_c \left| \frac{dH_{c2}}{dT} \right|_{T_c}}$ and ψ being the digamma functions) and they are well reproduced
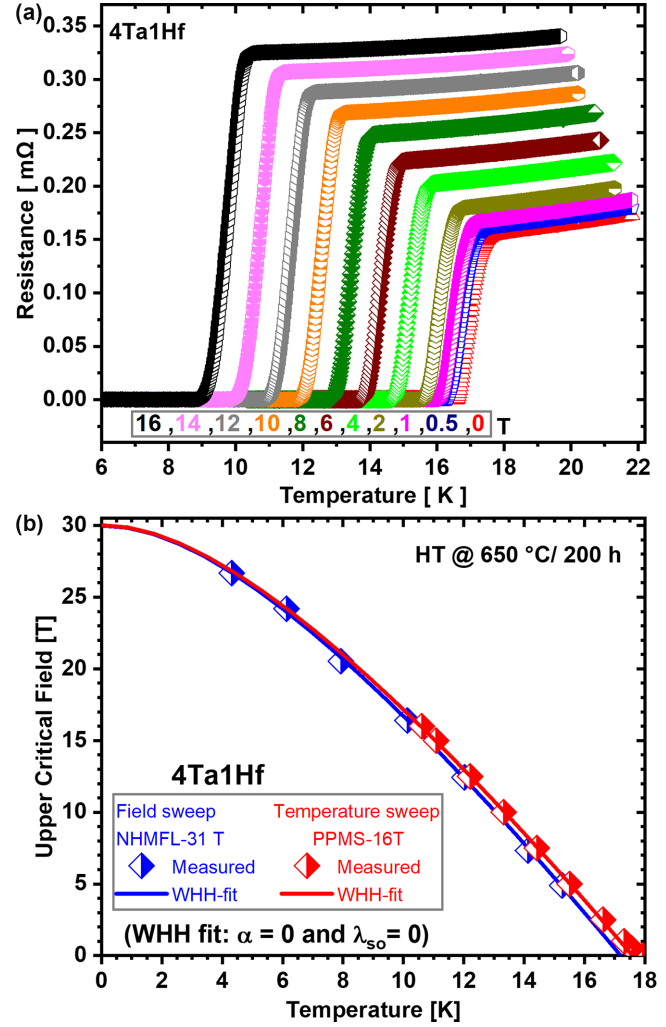
FIG. 6. (a) The traces of resistance against temperature using temperature sweeps at constant field from 0 to 16 T in our 16 T PPMS for Nb4Ta1Hf reacted at 550 °C/50 h+650 °C/200 h. (b) At the bottom we show the experimental $H_{c2}(T)$ values and their WHH fits in PPMS 16 T and NHMFL 31 T.

with the paramagnetic limitation parameter (α) and a spin-orbit scattering parameter (λ_{so}) both set to 0. This implies that the Nb_3Sn data can be fitted with the reduced $\ln \frac{1}{t} = \psi(\frac{1}{2} + \frac{\bar{h}}{2t}) - \psi(\frac{1}{2})$ relation. In the following data discussions, the parameters derived from the WHH fits are marked with a "WHH" superscript (e.g., T_c^{WHH}). The WHH theory predicts that for $\alpha = 0$ and $\lambda_{so} = 0$, the 0 K limit is given by the relation $H_{c2}(0) \sim 0.693 \, T_c \left| \frac{dH_{c2}}{dT} \right|_{T_c}$. This simpler expression instead of the full WHH fit has been widely used to estimate $H_{c2}(0)$ values of many superconductors since all it requires is to measure the H_{c2} slope in the higher-temperature, lower-field limit. There are, however, some experimental concerns when numerically accurate predictions are needed. Many samples have compositional variations for various reasons, as is the present case, because Nb_3Sn is not a line compound and, when made by diffusion, as here, composition gradients are always present. Because of the different dependences of T_c and H_{c2} on composition, this may lead to non-WHH H_{c2} behavior near T_c. Since we have to take this into account

TABLE I. A15 superconducting parameters for samples reacted at 550 °C/100 h+/100 h and 550 °C/50 h+/50 h (experimental and fitting parameter errors are typically defined by the last indicated digit).

Sample ID	$T_{c,\mathrm{exp}}$ (K) 670 °C/100 h	$T_{c,\mathrm{exp}}$ (K) 750 °C/50 h	T_c^{WHH} (K) 670 °C/100 h	T_c^{WHH} (K) 750 °C/50 h	$\mu_0 H_{c2}^{\mathrm{WHH}}(0)$ (T) 670 °C/100 h	$\mu_0 H_{c2}^{\mathrm{WHH}}(0)$ (T) 750 °C/50 h	$\mu_0 \left|\frac{dH_{c2}^{\mathrm{WHH}}(0)}{dT}\right|_{T_c}$ ($\frac{\mathrm{T}}{\mathrm{K}}$) 670 °C/100 h	$\mu_0 \left|\frac{dH_{c2}^{\mathrm{WHH}}(0)}{dT}\right|_{T_c}$ ($\frac{\mathrm{T}}{\mathrm{K}}$) 750 °C/50 h
4Ta	17.31	17.72	17.24	17.40	29.0	28.9	2.43	2.40
2Ta	17.61	18.15	17.49	17.86	28.2	28.5	2.33	2.31
4Ta1Hf	17.18	17.77	17.19	17.59	30.2	29.2	2.54	2.40
4Ta2Hf	17.57		17.46		29.7		2.46	
2Ta1Hf	16.96	17.87	16.99	17.69	28.3	28.8	2.40	2.35
2Ta2Hf	17.32	18.08	17.30	17.81	29.4	28.9	2.45	2.34
4Ta1Zr	17.44		17.36		30.0		2.49	
2Ta1Zr	16.99	17.72	16.98	17.53	27.9	27.9	2.37	2.30
2Ta2Zr	17.35	17.85	17.35	17.69	29.3	28.7	2.44	2.34
2Ta0.5Hf0.5Zr	17.24	17.81	17.23	17.62	29.2	28.7	2.45	2.35
2Ta1Hf1Zr	17.20	17.94	17.27	17.73	29.0	28.6	2.42	2.33
1Hf	17.17	17.75	17.11	17.52	27.9	27.2	2.35	2.24
3Hf	17.38	18.03	17.34	17.66	27.4	26.9	2.28	2.20
5Hf	17.49	17.85	17.41	17.51	28.0	26.1	2.32	2.15
0.8Ti	17.67		17.52		26.8		2.21	
0.8Ti4Ta	17.34		17.22		27.7		2.32	
0.8Ti1Hf	17.10		17.03		26.8		2.27	

to analyze our data, we explain in detail what causes these possible anomalies and the method we used to analyze our H_{c2} data within the WHH framework.

In inhomogeneous, varying composition samples both a T_c and an H_{c2} distribution result. Since typically the sample fraction with the highest T_c is closer to stoichiometry, it does not necessarily produce the highest H_{c2} at the lowest temperature. The result is thus a crossover in the $H_{c2}(T)$ trends of different portions of the A15 layer, which may produce a mild upward curvature near T_c, instead of a completely linear $H_{c2}(T)$. An H_{c2} slope determined in this upturn region would inevitably underestimate the H_{c2} slope of the sample fraction that generates the highest low-temperature H_{c2}, so we did not use this approach. Moreover, properly evaluating the H_{c2} slope near T_c is also difficult for homogeneous samples. In fact, according to the WHH relation, a linear fit of a range above $t = 0.9$ causes an underestimation of the slope of ~2%, which increases at ~4% if fitted above $t = 0.8$. For these reasons, to exclude a possible effect of an upward curvature near T_c, we prefer to analyze our $H_{c2}(T)$ results with the WHH fits but only on data at $\mu_0 H \geqslant 2$ T. The correctness of this approach is confirmed by both the quality of the fits and the closeness of the fitting parameter T_c^{WHH} to the experimentally evaluated $T_{c,\mathrm{exp}}$, reported in Table I. As expected, T_c^{WHH} is within the experimental error of $T_{c,\mathrm{exp}}$ or only slightly smaller, indicating minor inhomogeneity in only a few samples. As presented below, from the WHH fits we determine the essential parameters T_c^{WHH} and $|dH_{c2}^{\mathrm{WHH}}/dT|_{T_c}$ [or equivalently $H_{c2}^{\mathrm{WHH}}(0)$]. The value of determining and comparing the H_{c2} slopes, which is a convolution of γ and ρ_n, will be discussed in Sec. IV.

1. Effects of alloy dopants

To better understand how the dopants affect the different properties, we plotted in Fig. 7 the T_c^{WHH} data as a function of the total percentage of dopants in the unreacted alloys and for

clarity we separated the different trends into multiple panels: the data in the top panels are for an A15 reaction at 670 °C, whereas those in the bottom row are obtained after a 750 °C reaction. The left panels show the effect of Hf by itself or with fixed Ti, and the effect of Ti at fixed Ta. The middle panels report the effect of Ta by itself or when added to a fixed amount of Hf or Zr. The right panels represent the effect of Hf, Zr, or a combination of the two when added to a fixed amount of Ta. Equivalent data for the slope of H_{c2}^{WHH} and $H_{c2}^{\mathrm{WHH}}(0)$, described in the following are reported similarly in Figs. 8 and 9. The effects of dopants on T_c^{WHH} are quite complex and not always monotonic, but a general feature is that T_c^{WHH} increase with increasing the reaction temperature; the maximum difference (0.7 K) is observed in the 2Ta1Hf case.

Adding Hf to Ti is clearly detrimental [Fig. 7(a)], whereas adding Hf by itself has a peculiar effect. With only 1% Hf T_c^{WHH} is clearly depressed from the typical ~18 K of the binary Nb_3Sn, but it recovers at a higher Hf level for the 670 °C heat treatment [Fig. 7(a)]; at 750 °C T_c^{WHH} is higher than at 670 °C but nonmonotonic [Fig. 7(b)]. In our sample we also observed a decrease of T_c^{WHH} with increasing the Ta content by itself from 2% to 4% [Figs. 7(c) and 7(d)], whereas increasing Ta in combination with a fixed amount of Hf or Zr is beneficial to T_c^{WHH} or causes small suppression [Figs. 7(c) and 7(d)]; none of these double-doped wires have, however, a better T_c of the 2Ta wire. A very interesting trend is observed when increasing the Hf, Zr, or Hf-Zr content in the presence of a fixed amount of Ta [Figs. 7(e) and 7(f)]. In almost all cases (with the exception of 4Ta/4Ta1Hf at 750 °C) the trends show a V shape: in fact, the good T_c^{WHH} observed for xTa is reduced by adding 1% of other dopants to Ta (i.e., 2Ta1Hf, 4Ta1Hf at 670 °C only, 2Ta1Zr or 2Ta0.5Hf0.5Zr), whereas adding 2% of other dopants increases T_c^{WHH} again.

Increasing the reaction temperature causes a decrease of the H_{c2} slope in all cases, so an opposite behavior with respect to T_c^{WHH} (Fig. 8). Hf addition to Nb0.8Ti increases the
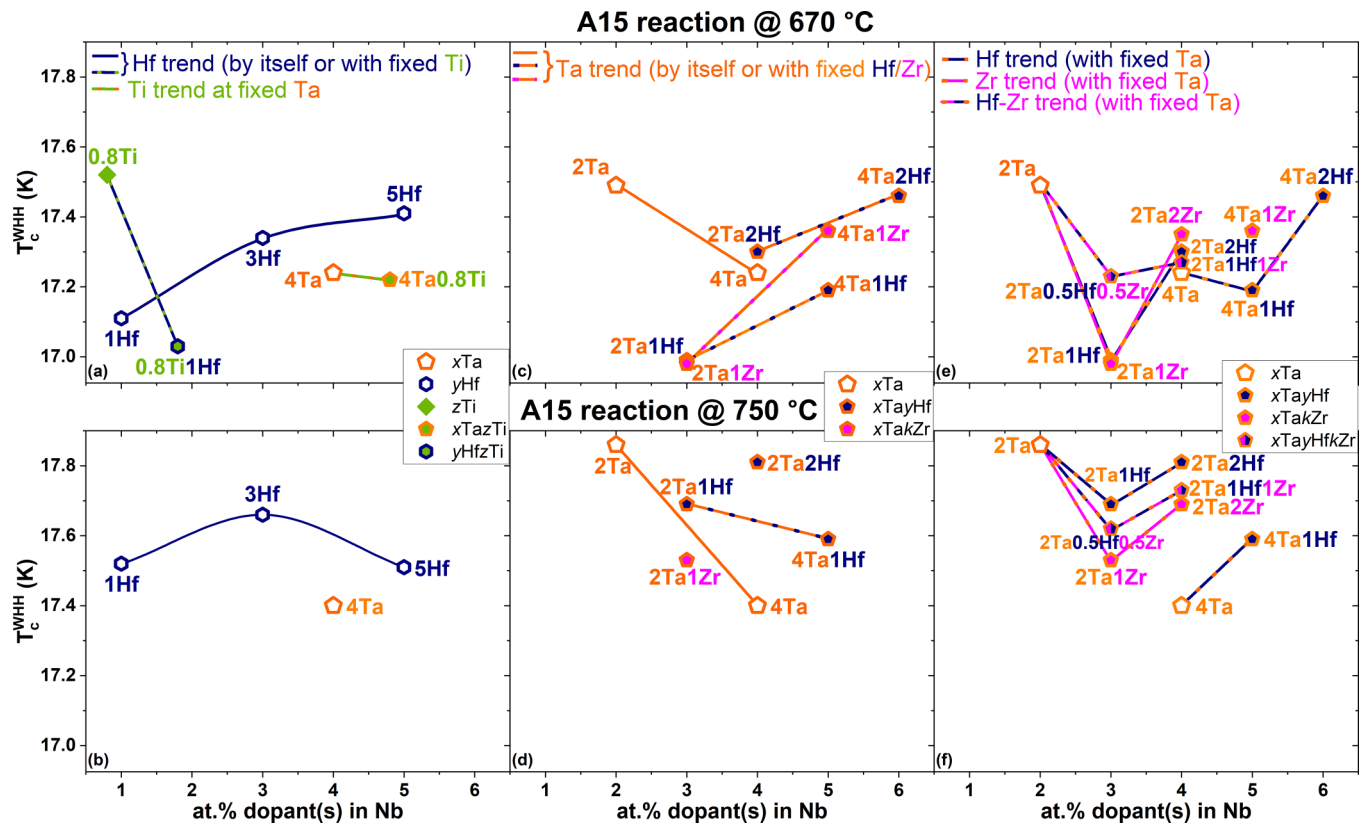
FIG. 7. T_c evaluated by the WHH fits for alloyed A15 samples reacted at 550 °C/100 h+670 °C/100 h (top row) and at 550 °C/50 h+750 °C/50 h (bottom row) as a function of the amount of dopant(s). For clarity the data has been organized into three columns [(a)-(b), (c)-(d), and (e)-(f)] of alloy sets with relevant fixed versus variable element concentrations. As explained in the text, the labels refer to the total atomic percentage of dopant(s) in the unreacted Nb alloys. It is immediately obvious that the trends are not the same at the two reaction temperatures.

H_{c2} slope, whereas the Ti addition to the Nb4Ta decreases it [Fig. 8(a)]. Increasing the amount of Hf by itself has a small nonsystematic variation on the H_{c2}^{WHH} slope at 670 °C, but it is clearly detrimental at 750 °C. Significantly higher values of $|dH_{c2}^{\mathrm{WHH}}/dT|_{T_c}$ are obtained for various combinations of Ta, Hf, and/or Zr at 670 °C. Figure 8(c) reveals that increasing the Ta content by itself or in the presence of Hf or Zr increases the slope: in fact, it increases from 2.33 to 2.43 T/K going from 2Ta to 4Ta. In the presence of 1Zr, the Ta trend at 670 °C is similar to that induced by the Ta only, reaching 2.49 T/K in the 4Ta1Zr case. Better is the trend found for Ta in combination with Hf, with a slope that increases from 2.40 to 2.54 T/K going from 2Ta1Hf to 4Ta1Hf, with the latter being the highest value of all. In the presence of 2Hf, increasing Ta has no significant impact. At 750 °C [Fig. 8(d)], the behavior is different and the presence of Hf or Zr has limited or no effect in increasing $|dH_{c2}^{\mathrm{WHH}}/dT|_{T_c}$ with respect to the only Ta trend. Looking at the trends with fixed Ta amount [Figs. 8(e) and 8(f)], adding an increasing amount of Hf or Zr to the 2Ta-base alloy is beneficial for the H_{c2}^{WHH} slope at 670 °C [with Hf being the more effective, Fig. 8(e)], whereas adding Hf and Zr together to the 2Ta base has a nonmonotonic behavior (inverted V shape) with the 2Ta0.5Hf0.5Zr (2.45 T/K) being better than 2Ta (2.33 T/K) and 2Ta1Hf1Zr (2.42 T/K). A similar nonmonotonic trend is also observed for the 4TayHf

series at 670 °C. Smaller and nonmonotonic variations are found at 750 °C [Fig. 8(f)].

Since we are ultimately interested in the low-temperature performance, it is important to also verify the trends in $H_{c2}^{\mathrm{WHH}}(0)$, which is proportional to T_c^{WHH} and $|dH_{c2}^{\mathrm{WHH}}/dT|_{T_c}$. Figure 9 shows that, except for 2Ta1Hf (+0.5 T), 2Ta1Zr (no difference), and the xTa series (small variations), all other samples reacted at 750 °C have a lower $H_{c2}^{\mathrm{WHH}}(0)$ than those at 670 °C. At the lower reaction temperature [Fig. 9(a)], Hf by itself or in combination with Ti do not generate high $H_{c2}^{\mathrm{WHH}}(0)$ (28 T maximum) and 5Hf at 750 °C causes the strongest H_{c2} suppression [26.1 T in Fig. 9(b)]. 4Ta leads to an $H_{c2}^{\mathrm{WHH}}(0)$ of 29 T, compared to 28.2 T for 2Ta [Fig. 9(c)]. In the presence of 1% Hf [Fig. 9(c)], H_{c2} is enhanced much more markedly, going from 2Ta1Hf (28.3 T) to 4Ta1Hf (30.2 T); adding 1% Zr to xTa produces a similar trend but with slightly lower $H_{c2}^{\mathrm{WHH}}(0)$ than with the Hf (27.9 and 30.0 T in 2Ta1Zr and 4Ta1Zr, respectively). The xTa2Hf series is clearly better than the xTa one [Fig. 9(c)], but it does not reach the performance of 4Ta1Hf or 4Ta1Zr. At 750 °C [Fig. 9(d)] the trends are closer and mostly determined by the total dopant content, with the exception of 2Ta1Zr that has a lower $H_{c2}^{\mathrm{WHH}}(0)$ with respect to all other samples.

Changing the Hf, Zr, or Hf+Zr content in the 2Ta and 4Ta bases [Figs. 9(e) and 9(f)] produced nonmonotonic
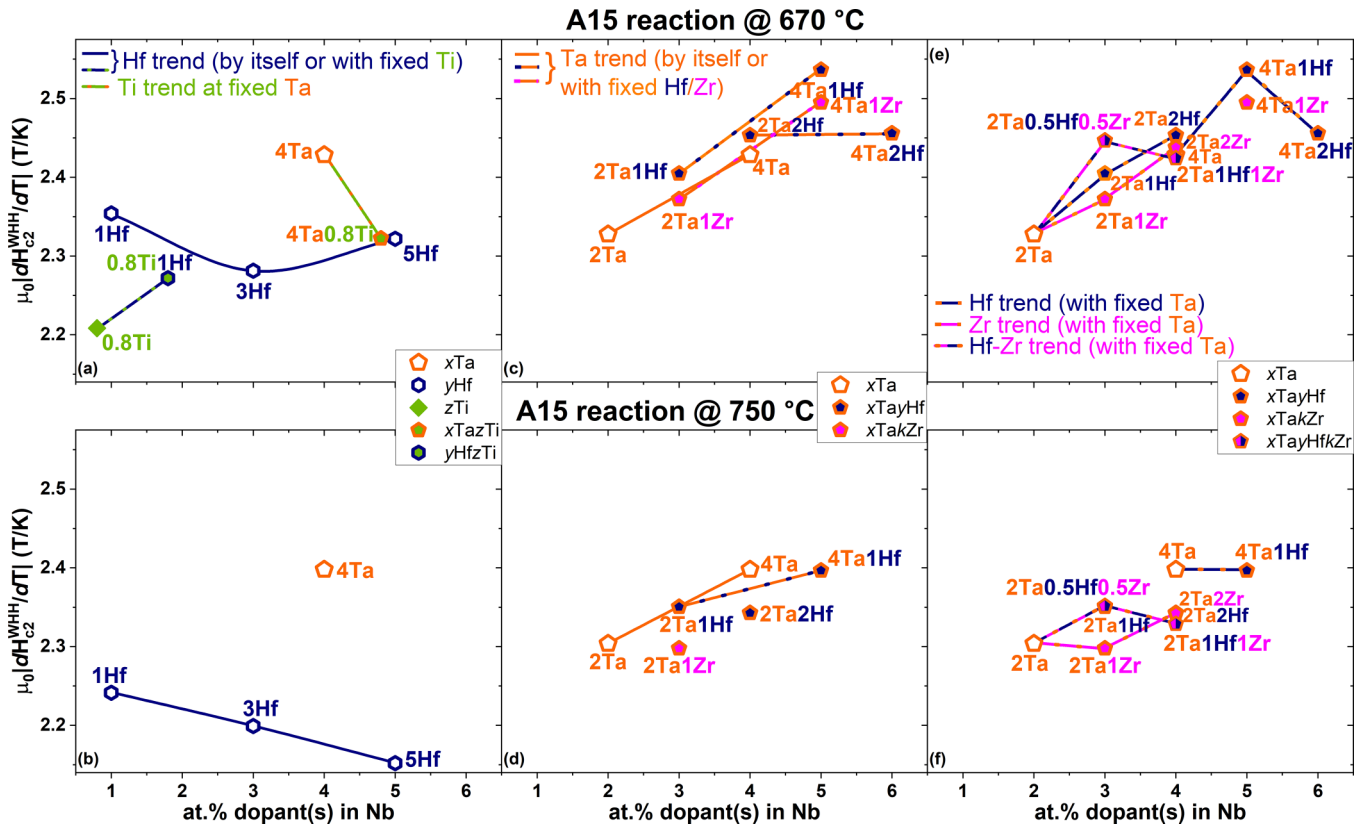
FIG. 8. H_{c2} slope evaluated by the WHH fits for alloyed A15 samples reacted at $550\,°C/100\,h+670\,°C/100\,h$ (top row) and at $550\,°C/50\,h+750\,°C/50\,h$ (bottom row) as a function of the amount of dopant(s). The same alloy sets as used for the (a)-(b), (c)-(d), and (d)-(e) columns in Fig. 7 are used for the column sets here. As explained in the text, the labels refer to the atomic percentage of dopant(s) in the unreacted Nb alloys.

behaviors in all $670\,°C$ cases, although with different trends depending on whether T_c^{WHH} or the H_{c2}^{WHH} slope dominates. The best $H_{c2}^{\mathrm{WHH}}(0)$ is reached in 4Ta1Hf, and a further increase of Hf is not beneficial. A total of 4% of dopants (4Ta, 2Ta2Hf, 2Ta2Zr, or 2Ta1Hf1Zr) produces a relatively small variation in $H_{c2}^{\mathrm{WHH}}(0)$ in both reactions (29–29.4 T at $670\,°C$ and 28.6–28.9 T at $750\,°C$). Overall, despite the spreading on the data, Fig. 9 shows that (excluding Ti and single Hf additions) there is an almost monotonic increase in $H_{c2}^{\mathrm{WHH}}(0)$ with increasing overall dopant content up to 5 at. %, whether by Ta alone or by Ta+Hf, Ta+Zr, or Ta+Hf+Zr combinations.

2. Effects of reaction temperature on Ta-base samples

To better understand the effect of the reaction temperature on H_{c2}, we varied the A15 reaction temperature from $650\,°C$ to $750\,°C$ and determined the resulting T_c values and H_{c2}^{WHH} slope for the xTa ($x = 2, 4$) base samples as summarized in Fig. 10. In both cases, T_c monotonically increases with increasing reaction temperature, whereas the H_{c2}^{WHH} slopes either have a small variation or they decrease. These substantially opposite trends lead to a $H_{c2}^{\mathrm{WHH}}(0)$ that is always better for the 4Ta case but with an almost constant value at $670\,°C$ and $750\,°C$ reaction temperatures for both 2 at. % and 4 at. % Ta doping levels.

3. Effects of Ga addition

Our experiments on the effect of including Ga in the Cu-Sn mixture did not reproduce earlier high claims and in fact revealed a significantly negative impact on both the A15 reaction temperature and T_c values. By incorporating 20 at. % Ga into a Cu-Sn powder mixture, we observed an onset T_c of only 13 K, which also required the unreasonable reaction temperature of $1100\,°C$; T_c values below 9.5 K were obtained for all heat treatments below $1100\,°C$. To improve these results, we decreased the amount of Ga in the Cu-Sn powder mixture to 2 at. %, resulting in a lower A15 reaction temperature of $800\,°C−850\,°C$. The microstructures of the A15 reaction layer are shown in Figs. 11(a) and 11(b), clearly revealing the formation of Hf-rich precipitates at these high temperatures with an increase in their size and density as the A15 reaction temperature is increased. Our observations also revealed that the A15 grains in Ga-Ta-zHf wires coarsened immediately after the onset of A15 formation, while in Ta-Hf wires, the grain size was refined to as small as 70 nm [32]. These reaction temperatures are significantly higher than typically employed for magnets ($650\,°C − 670\,°C$), but they were necessary to obtain relatively homogeneous samples with good T_c. In Fig. 11(c) we compare $H_{c2}(T)$ for the 4Ta1Hf wires made with and without Ga and reacted at the same temperature of $850\,°C$. The two samples have comparable $H_{c2}^{\mathrm{WHH}}(0)$ of 28.5–28.6 T.
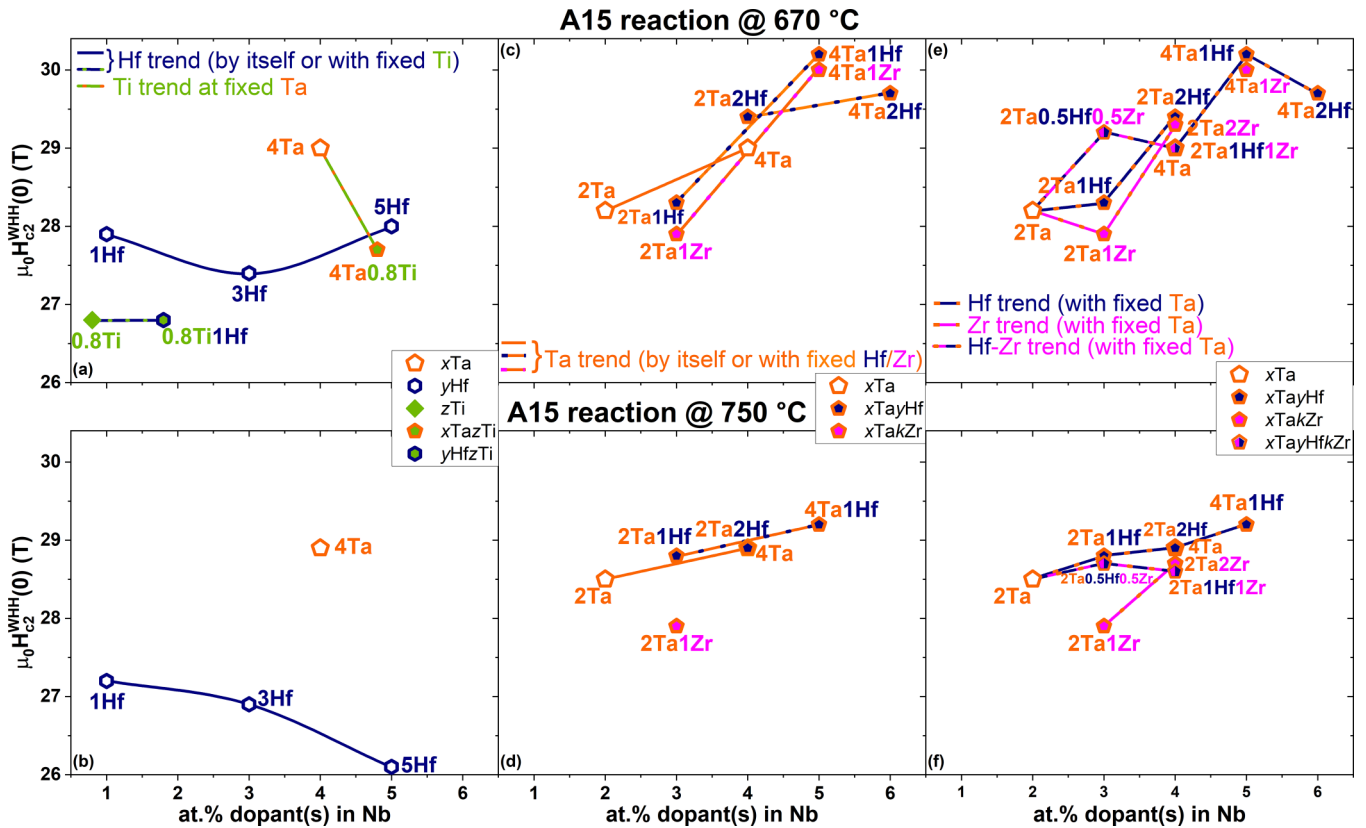
FIG. 9. $H_{c2}(0)$ evaluated by the WHH fits for alloyed A15 samples reacted at $550\,°C/100$ h+$670\,°C/100$ h (top row) and at $550\,°C/50$ h+$750\,°C/50$ h (bottom row) as a function of the amount of dopant(s). The same alloy sets as used for the (a)-(b), (c)-(d), and (d)-(e) columns in Fig. 7 are used for the column sets here. As explained in the text, the labels refer to the atomic percentage of dopant(s) in the unreacted Nb alloys.

This is, however, 2 T below the maximum $H_{c2}^{\mathrm{WHH}}(0)$ obtained on 4Ta1Hf without Ga at the much lower reaction temperature of $670\,°C$.

IV. DISCUSSION

A. Overview and value of a new H_{c2} study

In the production of Nb$_3$Sn conductors, the addition of Ta and Ti has been a common practice since the 1980s [16,25,36]. The choice between using titanium or tantalum was originally the practical one of whether the commercial Nb 0.8 wt % Ti or Nb 7.5 wt % Ta alloy was cheaper or more available. After it was found that replacing a few of the more widely available pure Nb filaments with standard Nb 47 wt % Ti filaments enabled effective Ti doping throughout the wire [37,38], Ti doping largely replaced Ta as dopant in rod-based conductors like RRP, although Nb 7.5 wt % Ta (Nb4Ta) was still favored for PIT conductors [9,39,40]. According to Suenaga both elements have a similar effect on raising H_{c2} [16].

However, the new FCC target specification [41] explicitly links the need for the highest possible critical current density (J_c), which is encouraged by the smallest possible A15 grain size, to the need for the highest possible H_{irr} and H_{c2}. This new perspective forces alloying strategy to consider both demands in addition to the internal oxidation approach [30,32,33].

This paper focuses on two aspects of the effect of alloying Nb with Ti, Ta, Zr, and/or Hf, and the use of Ga: (1) the recrystallization behavior of the Nb alloy, which, if delayed above the normal A15 reaction temperature, sets up a denser nucleation of the growing A15 phase; and (2) the upper critical field of the resulting Nb$_3$Sn A15 layers. We note at the outset that H_{c2} alloying has been studied by many others, but generally only a few alloys at a time and often with limited access to high fields. This leads to difficulties in making reliable comparisons between studies and in understanding what properties are controlling changes in H_{c2} as we discuss in the next section. The specific challenges of meeting the FCC specification are what prompted this systematic comparative study of alloys from one single source [32]. A common observation is that small alloy additions cause H_{c2} to increase, likely because the alloying element creates disorder in the A15 compound [13,26]. The relationship between increased alloying and higher H_{c2} may depend on whether the dopant enters the A15 lattice and which site it then occupies.

An essential study for explaining alloying effects in binary alloys is the thin film H_{c2} study of Orlando *et al.* [10]. One view is that binary Nb$_3$Sn is always ordered [13,42], meaning that Sn-deficient A15 has the Nb chain sites always occupied by Nb atoms with vacant Sn sites as appropriate to the Sn content which can vary from 18 to 25 at. % Sn. More recent calculations of the energetics of disorder in the A15 lattice by Besson *et al.* disagree with this view [43], concluding that
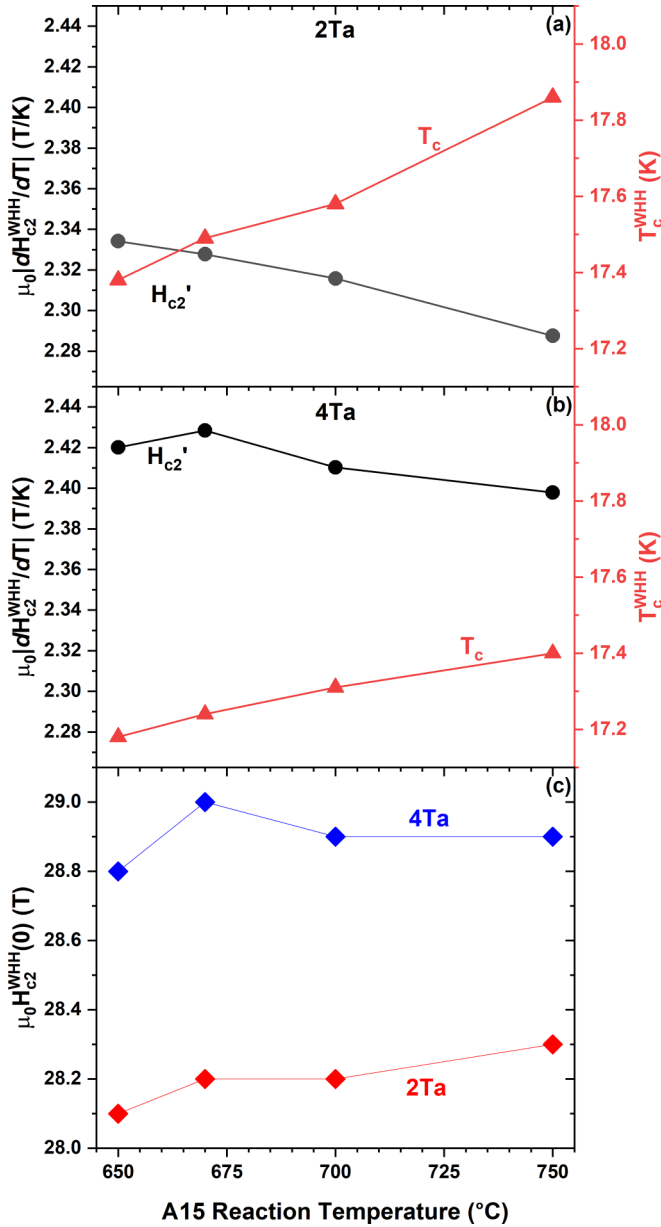
FIG. 10. Variation of $|dH_{c2}^{WHH}/dT|_{T_c}$ and T_c^{WHH} in the (a) 2Ta and (b) 4Ta wires as a function of A15 reaction temperature. (c) Variation of $H_{c2}^{WHH}(0)$ for both sample series.

FIG. 11. FESEM-BSE images of the Ga+4Ta1Hf wires made with Nb4Ta1Hf + Cu-Ga-Sn and reacted at (a) 800 °C, (b) 850 °C, and (c) WHH fit of the upper critical field for the Ga+4Ta1Hf reacted at 550 °C/50 h+/96 h. SEM-EDXS analysis shows up to 1.7 at. % Ga in the A15 layer at 850 °C. The $H_{c2}(0)$ of Ga+4Ta1Hf reacted at 850 °C are 2 T lower than for 4Ta1Hf without Ga reacted at much lower temperature (670 °C).

antisite disorder in substoichiometric compositions is preferred. We do note that the Sn-deficient binary thin film made by Orlando *et al.* [10] with the highest $H_{c2}(0)$ of 29 T had a high resistivity of 36 µΩ cm and suppressed T_c of 16.1 K, both suggestive of strong disorder.

In the alloyed A15 compositions of today's Ti- and Ta-optimized wires, disorder is complicated because we must consider where Ta and Ti sit. To address the common finding that optimum, high-J_c Ti-doped wires generally always had Sn-deficient A15 compositions (a maximum of ∼ 23 at. % Sn), EXAFS studies on commercial Ta, Ti, and Ta+Ti RRP standard wires showed that Ta substitutes on both Nb and Sn sites but with a dependence on the heat treatment temperature, whereas Ti substitutes only on Nb sites independent of the reaction temperature [18,19]. However, this

rather unexpected result is consistent with the result that Ti is about twice more effective (<2 at. % Ti versus 4 at. % Ta) per atomic percentage in raising H_{c2}. This implies that Ti preferentially produces disorder on the Nb A15 lattice sites, while Ta sitting on both Sn and Nb sites is a less potent disordering agent. Future EXAFS studies with bulk samples are planned to address this speculation in greater detail.

B. Hardness, drawability, recrystallization of Nb alloys and effect of alloying on A15 grain refinement

It was previously reported that Nb5Hf and Nb5Zr were sufficiently ductile for wire fabrication [27], a result which is confirmed here: in fact, we saw that all the Nb dopants work hardened the alloy but not as much as is the case for the world's most heavily produced superconductor, Nb 47 wt % Ti [44]. We have separately evaluated the ductility of the Nb4Ta1Hf alloy in commercially produced tubes, finding that it remains ductile for true drawing strains as high as 15 that enabled 22-mm-diameter tubular filaments [44,45]. Work hardening is generally most strongly affected by the size differential between the added solute and the matrix, Nb, which has a metallic atomic radius of 0.142 nm. The largest dopant was Hf (radius 0.160 nm) followed by Zr (0.160 nm), Ta (0.143 nm), and Ti (0.142 nm), respectively. In this respect

the greater work hardening exhibited by Zr and Hf is entirely expected.

Our observations indicate that the introduction of larger atoms like Hf and Zr and an increase in their concentration results in significant hardening of the Nb alloy, which is consistent with standard solid solution strengthening mechanisms. The hardness exhibits a near-linear increase with alloy content, as shown in Fig. 2. Our Vickers hardness study revealed that the initial rate of increase in hardness is greater than that observed after a true strain $\varepsilon = 3.5$. To evaluate the drawability and recrystallization temperature of the commercial Nb4Ta alloy and arc-melted Nb4Hf custom alloy, both alloys were annealed at up to 1000 °C for 3 h after true strains of 7.0 and 8.1. The study shows that Nb4Hf increases the recrystallization temperature to ∼800 °C, in contrast to the Nb4Ta base alloy which was already recrystallized at 650 °C, as shown in Fig. 3. The significance of adding Hf to increase the recrystallization temperature is emphasized by these findings.

Since unreacted Nb alloy remained in the core following the A15 monofilament reaction, the FESEM-BSE image analysis showed that recrystallization of the NbxHf ($x = 1, 3$), Nb2TaxHf (Zr) ($x = 1, 2$), Nb2Ta(xHfxZr) ($x = 0.5, 1$) alloys is always delayed until 750 °C. On the other hand, Fig. 5 shows that NbxTa ($x = 2, 4$), Nb4Ta0.8Ti, and Nb0.8Ti fully recrystallize at 750 °C. Incorporating the larger atoms of Hf or Zr, or a combination of both, into Ta does refine the A15 grain size during standard reactions [32,33]. It should be noted that the Nb-alloy recrystallization temperature increases with larger dopant atom sizes. Achieving this is extremely beneficial for A15 grain refinement, as the core alloy's grain structure directly affects the A15 nucleation. The higher recrystallization temperature enables more effective refinement of the A15 grain structure, resulting in better high-field performance of the Nb$_3$Sn conductor [32,33]. Qualitative analysis of FESEM-BSE images demonstrated that the addition of Hf (Zr) to NbxTa ($x = 2, 4$) alloys refines the grain size of the A15 phase (Fig. 5).

C. WHH fit to estimate $H_{c2}(T)$

Figure 6 shows a good agreement between the experimental data and the WHH fits for data taken both up to 31 T and in our 16 T system. This agreement has a very important practical implication: Since measurements performed in fields up to 16 T [about 0.5 $H_{c2}(0)$ are sufficient to provide a good estimate of $H_{c2}(0)$ without a need for characterizations in high-field facilities of limited access, a wide-range study of many alloys can be performed with limited field as here, where measurements in the NHMFL 31 T magnet was possible only for a few samples. Moreover, similarly to what was found by Orlando *et al.* for binary samples, we verified that H_{c2} curves can be fitted without taking into account the Pauli paramagnetic limitation also for our ternary and quaternary A15 wires [46], as expected, considering that in all cases $H_{c2}(0)$ does not exceed the zero-temperature BCS Pauli limit $\mu_0 H_{p,\mathrm{BCS}}(0) = 1.86 T_c$. For instance, the range of $H_{p,\mathrm{BCS}}(0)$ for the alloyed samples listed in Table I (considering the T_c^{WHH} values) is ∼31.6–33.2 T, with $H_{p,\mathrm{BCS}}$ up to 6.5 T larger than H_{c2}. The sample whose $H_{c2}(0)$ most closely approaches

$H_{p,\mathrm{BCS}}(0)$ is the 4Ta1Hf wire heat treated at 670 °C, where the difference is reduced to only ∼1.8 T. Moreover, in Nb$_3$Sn the effect of strong coupling should probably be taken into account leading to an H_p enhanced by a factor $\eta_{H_c}(1 + \lambda_{ep})^{1/2}$ with respect to the BCS value (from Orlando *et al.* [46]).

D. Optimizing H_{c2} by increasing disorder

The $H_{c2}(0)$ of clean A15 wires is typically 25–26 T [47]: however, it is possible to reach values of up to 30 T in binary alloys using a variety of methods [48]. This suggests that disorder, likely in the Nb chain sites, is the main mechanism controlling H_{c2}. Earlier studies on bulk Nb-Sn samples have revealed that a normal state resistivity (ρ_n) value between 25 and 30 μΩ cm can result in H_{c2} values up to 30.0 T [10,48]. These values correspond to a H_{c2} slope of $2.40 - 2.50$ T/K and a T_c range of $17.0 - 17.3$ K. It is important to note that T_c remains constant up to 20 μΩ cm but drops rapidly above 30 μΩ cm, which significantly degrades H_{c2} [10]. Since the H_{c2} slope is proportional to $\gamma \rho_n$, increasing disorder without losing too much T_c is key to optimizing the H_{c2} performance. Typically, the slope increases with ρ_n up to 2.5 T/K, then decreases [10,46] and in Ta+Ti-doped samples, the maximum H_{c2} was obtained for a ρ_n value of around 35 μΩ cm [13]. Unfortunately, like almost all wires whether made in a laboratory as here or commercially, it is not possible to separately measure γ and ρ_n. Therefore, here we focused on the influence of doping on the H_{c2} slope and T_c, knowing that the optimal low-temperature performance is achievable by maximizing the first without losing too much T_c.

In our samples, we found that T_c usually slightly increases with increasing reaction temperature, likely due to increased diffusivity of Sn into the growing A15 layer which becomes more homogeneous. However, this increased temperature is not beneficial for the disorder, as the H_{c2} slope systematically decreases in all samples after increasing the reaction temperature to 750 °C. This is also true for the Nb4Ta alloy, which was investigated in a wide reaction temperature range. The combined opposite effects of the reaction temperature on T_c and the H_{c2} slope leads to a mostly detrimental or negligible effect on $H_{c2}(0)$. We notice that this trend is different from that found in Ta-doped RRP [7,19] where increasing reaction temperature increases both H_{c2} and the Kramer field (although with some weakening of the pinning performance). The different behaviors could be caused by the different wire designs, which could affect both the reaction path and the Sn diffusivity into the Nb alloy, affecting in turn the Ta occupancy. As verified by EXAFS studies, in RRP Ta occupies more Sn sites after a low-temperature reaction, when the Sn supply is low, limiting the disorder on the Nb chains, whereas, when the Sn diffusivity is enhanced, Ta occupies mostly the Nb sites. Since in the present wires the Sn source is outside diffusing inward into the Nb alloy, the Sn supply in late stages of the reaction could be better than in RRP (where Sn diffuses outward), so leading to more Ta occupying the Nb sites already at a low reaction temperature.

Looking instead at the effect of the dopant concentration, we found that T_c is suppressed with increasing Ta content in Ta-only alloyed wires, but with a corresponding increase of the low-temperature H_{c2}: this is consistent with the behavior

previously observed by Suenaga [16], which also found the maximum T_c at 2% Ta and the maximum H_{c2} at ~4%Ta.

Additions of Ti or Hf by themselves or together is instead not beneficial for the low-temperature H_{c2} performance, indeed producing the worst $H_{c2}(0)$ values of our sample set. For Ti, this behavior is different from earlier reports showing that 0.8 Ti optimizes H_{c2} [16]. The depressed H_{c2} of our Ti-doped samples could be caused by the absence of Ti in the A15 structure. In fact, although in other Ti-doped Nb_3Sn samples Ti substitutes into the A15 structure, in our case the FESEM analysis reveals some dark-contrast areas [Fig. 5(c)]: Although they were too small to perform FESEM-EDS chemical characterization, the low BSE intensity is consistent with low atomic number Ti-rich precipitates. The worsening effect of Hf on H_{c2} as the atomic percentage of Hf increases at 750 °C may be due to Hf precipitating out of the alloy (Fig. 4) and not entering the A15 phase. Suenaga observed Hf-Sn precipitates in bronze-process wire and suggested this to be the primary reason for the relatively small benefit of Hf on H_{c2} in comparison with Ta and Ti [16].

More interesting are the effects of combining different elements, like Ta, Hf, and/or Zr. Although adding Hf or Zr to the Ta-base alloy is not beneficial for T_c for the 2Ta, the double doping has a clear benefit in increasing the disorder as emphasized by the increase of the H_{c2} slope. This leads to better $H_{c2}(0)$ in wires with a total doping percentage (Ta+Hf or Ta+Zr), between 4% and 6% at 670 °C with the best performance observed in the 4Ta1Hf wire, followed closely by 4Ta1Zr, 4Ta2Hf, and 2Ta2Hf. Figure 8(c) shows that the H_{c2} slopes of xTa and xTa1Zr follow the same trend suggesting that the two elements similarly introduce disorder, possibly with similar occupancy, and only the total amount of dopants is relevant. On the other end the H_{c2} slope trend for xTa1Hf is clearly above that of xTa and xTa1Zr, suggesting that Hf and Ta synergistically increase disorder in the A15 phase. Interestingly, Ta has the same size as Nb, while Hf and Zr are larger, leaving it open for discussion whether, like their group IVB sibling Ti, they also only occupy the Nb site.

Furthermore, the reaction temperature may also play a significant role in determining H_{c2}. In standard Ta- or Ti-doped RRP wires, higher H_{c2} is always associated with higher reaction temperatures which make the A15 layer more Sn rich [7]. However, in some of these new alloys, a lower-temperature reaction yields higher H_{c2}, indicating that the relation between disorder and reaction temperature can also differ because of other factors. The lowering of $H_{c2}(0)$ by about 1 T for the highest H_{c2} Hf and Zr alloys for reactions at 750 °C rather than 670 °C leads us to speculate that, like Ti, their group IVB siblings, Zr and Hf, also sit on the Nb sites but may be vulnerable to being pushed off this site by Ta switching from Sn to Nb sites with increasing reaction temperature. Despite the $H_{c2}(0)$ suppression observed for the reaction temperature of 750 °C with respect to 670 °C, also at high temperature the 4Ta1Hf wire produces a larger H_{c2} slope than the other alloys.

We note that, despite the different efficiency, all these alloys introduce a significant amount of disorder as evidenced by the H_{c2} slope reaching 2.54 T/K, compared to only 1.85 T/K for the binary system [47]. However, this increase in slope does not translate to a corresponding increase in H_{c2}, primarily due to the suppression of T_c.

We also reexamined the effect of Ga addition to the Cu-Sn powder mixture but together with the Nb4Ta1Hf alloy. However, introducing 2 at. % Ga meant that a high A15 reaction temperature of 800 °C was required to form even a small amount of A15 (Fig. 11). At a temperature of 850 °C, the Ga-Hf samples underwent a full reaction, resulting in a complete annulus of A15 surrounding the core alloy but the high temperatures produced very large grains already at the onset of A15 formation as well as the formation of Hf precipitates. Comparable but depressed H_{c2} values of 28.5–28.6 T are obtained in these conditions for the Ga-Ta-Hf and Ta-Hf wires, almost identical to those previously estimated for the Nb-Hf/Cu-Ga-Sn system [27,36]. It is worth noting that the addition of Ta to Hf resulted in an enhanced $H_{c2}(0)$, while the addition of Ta to Ga-Hf had a minimal to no impact on $H_{c2}(0)$ values [27]. Previous studies by Bormann *et al.* [26] reported that $H_{c2}(0)$ could reach up to 33–35 T for a 1.5−2.0 at. % Ga addition to the binary A15 layer in coevaporated thin film samples (no Ta or Hf). In our samples, even though FESEM-EDXS analysis revealed the presence of 1.7 at. % Ga in the A15 layer, the H_{c2} value was low, consistent with its decreased H_{c2} slope. In short no evidence was found in this study to support earlier reports of a positive influence of Ga addition on H_{c2} [27].

H_{c2} is only one of the properties that determined the high-field performance of Nb_3Sn wires. Other superconducting characterizations (e.g., transport J_c) require the fabrication of multifilamentary, long and longitudinally uniform wires with a more suitable design and they will be studied in the future.

V. CONCLUSIONS

In conclusion, we showed that the addition of up to 5 at. % of Ta, Ti, Hf, Zr, or a combination of these elements to Nb does not negatively impact their drawability. Using Hf or Zr by themselves or in combination with Ta or Ti can help to delay the recrystallization temperature and refine the grain size of the A15 phase. The optimization of H_{c2} is temperature sensitive and likely influenced by changes in site occupancy and disorder. The best approach to maximize H_{c2} was to use a Nb4Ta base and add Hf or Zr, reaching a maximum $H_{c2}(0)$ of 30.2 T by using the Nb4Ta1Hf alloy and reacting the wire at 670 °C, closely followed by Nb4Ta1Zr leading to an $H_{c2}(0)$ of 30.0 T. Despite the $H_{c2}(0)$ enhancement, the WHH model without Pauli paramagnetic limiting can fit all our $H_{c2}(T)$ data, allowing us to characterize a variety of Nb alloys without a need for high-field measurements at 31 T. Unfortunately, the trend of the H_{c2} slope and T_c against A15 reaction temperature shows that it was not possible to simultaneously optimize these two parameters that determine $H_{c2}(0)$, producing almost constant $H_{c2}(0)$ in samples prepared with NbxTa (x = 2, 4 at. %). Moreover, increasing the reaction temperature rapidly degrades the H_{c2} performance of the Hf/Zr-doped samples. Our findings confirm the performance enhancing properties of Hf when combined with Nb4Ta, as recently reported by Balachandran *et al.* [32], without, however, providing further improvements. Contrary to earlier reports on Ga reaching $H_{c2}(0) \sim 33−35$ T, we observed a strong depression of $H_{c2}(0)$ with as little as 2 at. % Ga in a Cu-Sn powder mixture. Despite Nb_3Sn being the first high-field superconductor and remarkably still in

wide use even 60 years after the first demonstration of its high-field properties, it is clear that there is still much to learn about the limits of its high-field properties.

ACKNOWLEDGMENTS

[1] E. Todesco, M. Annarella, G. Ambrosio, G. Apollinari, A. Ballarino, H. Bajas, M. Bajko, B. Bordini, R. Bossert, L. Bottura *et al.*, Progress on HL-LHC Nb₃Sn magnets, IEEE Trans. Appl. Supercond. **28**, 4008809 (2018).

[2] L. D. Cooley, A. K. Ghosh, D. R. Dietderich, and I. Pong, Conductor specification and validation for high-luminosity LHC quadrupole magnets, IEEE Trans. Appl. Supercond. **27**, 1 (2017).

[3] J. A. Parrell, M. B. Field, Y. Zhang, and S. Hong, Nb₃Sn conductor development for fusion and particle accelerator applications, AIP Conf. Proc. **711**, 369 (2004).

[4] C. B. Segal, Performance limits of powder in tube processed Nb₃Sn superconducting wires, Ph.D. thesis, The Florida State University (2018).

[5] C. Sanabria, M. Field, P. J. Lee, H. Miao, J. Parrell, and D. C. Larbalestier, Controlling Cu–Sn mixing so as to enable higher critical current densities in RRP® Nb₃Sn wires, Supercond. Sci. Technol. **31**, 064001 (2018).

[6] D. Schoerling and A. V. Zlobin, Nb₃Sn *Accelerator Magnets: Designs, Technologies and Performance*, edited by D. Schoerling and A. V. Zlobin (Springer, Cham, 2019).

[7] C. Tarantini, P. J. Lee, N. Craig, A. Ghosh, and D. C. Larbalestier, Examination of the trade-off between intrinsic and extrinsic properties in the optimization of a modern internal tin Nb₃Sn conductor, Supercond. Sci. Technol. **27**, 065013 (2014).

[8] R. M. Scanlan, W. A. Fietz, and E. F. Koch, Flux pinning centers in superconducting Nb₃Sn, J. Appl. Phys. **46**, 2244 (1975).

[9] A. Godeke, M. C. Jewell, C. M. Fischer, A. A. Squitieri, P. J. Lee, and D. C. Larbalestier, The upper critical field of filamentary Nb₃Sn conductors, J. Appl. Phys. **97**, 093909 (2005).

[10] T. Orlando, J. Alexander, S. Bending, J. Kwo, S. Poon, R. Hammond, M. Beasley, E. McNiff, and S. Foner, The role of disorder in maximizing the upper critical field in the Nb-Sn system, IEEE Trans. Magn. **17**, 368 (1981).

[11] C. M. Fischer, Investigation of the relationships between superconducting properties and Nb₃Sn reaction conditions in powder-in-tube Nb₃Sn, Master's thesis, University of Wisconsin-Madison, 2002.

[12] H. Devantay, J. L. Jorda, M. Decroux, J. Muller, and R. Flükiger, The physical and structural properties of superconducting A15-type Nb-Sn alloys, J. Mater. Sci. **16**, 2145 (1981).

[13] R. Flükiger, D. Uglietti, C. Senatore, and F. Buta, Microstructure, composition and critical current density of superconducting Nb₃Sn wires, Cryogenics **48**, 293 (2008).

[14] L. J. Vieland, R. W. Cohen, and W. Rehwald, Evidence for a first-order structural transformation in Nb₃Sn, Phys. Rev. Lett. **26**, 373 (1971).

[15] C. Tarantini, Z.-H. Sung, P. J. Lee, A. K. Ghosh, and D. C. Larbalestier, Significant enhancement of compositional and superconducting homogeneity in Ti rather than Ta-doped Nb₃Sn, Appl. Phys. Lett. **108**, 042603 (2016).

[16] M. Suenaga, Optimization of Nb₃Sn, IEEE Trans. Magn. **21**, 1122 (1985).

[17] M. Suenaga, T. S. Luhman, and W. B. Sampson, Effects of heat treatment and doping with Zr on the superconducting critical current densities of multifilamentary Nb₃Sn wires, J. Appl. Phys. **45**, 4049 (1974).

[18] S. M. Heald, C. Tarantini, P. J. Lee, M. D. Brown, Z. Sung, A. K. Ghosh, and D. C. Larbalestier, Evidence from EXAFS for different Ta/Ti site occupancy in high critical current density Nb₃Sn superconductor wires, Sci. Rep. **8**, 4798 (2018).

[19] C. Tarantini, S. Balachandran, S. M. Heald, P. J. Lee, N. Paudel, E. S. Choi, W. L. Starch, and D. C. Larbalestier, Ta, Ti and Hf effects on Nb₃Sn high-field performance: Temperature-dependent dopant occupancy and failure of Kramer extrapolation, Supercond. Sci. Technol. **32**, 124003 (2019).

[20] V. Abächerli, D. Uglietti, B. Seeber, and R. Flükiger, (Nb, Ta, Ti)₃Sn multifilamentary wires using Osprey bronze with high tin content and NbTa/NbTi composite filaments, Physica C (Amsterdam, Neth.) **372**, 1325 (2002).

[21] V. Abacherli, D. Uglietti, P. Lezza, B. Seeber, R. Flukiger, M. Cantoni, and P.-A. Buffat, The influence of Ti doping methods on the high field performance of (Nb, Ta, Ti)₃Sn multifilamentary wires using Osprey bronze, IEEE Trans. Appl. Supercond. **15**, 3482 (2005).

[22] D. Dew-Hughes, Effect of third element additions on the properties of bronze processed Nb₃Sn, IEEE Trans. Magn. **13**, 651 (1977).

[23] M. K. Rudziak and T. Wong, Development of a Nb₃Sn conductor containing Ga and Mg dopants, IEEE Trans. Appl. Supercond. **11**, 3580 (2001).

[24] T. Takeuchi, T. Asano, Y. Iijima, and K. Tachikawa, Effects of the IVa element addition on the composite-processed superconducting Nb₃Sn, Cryogenics **21**, 585 (1981).

[25] W. Goldacker and R. Flükiger, Phase transitions and superconducting properties of binary and Ti, Ta, Ga and H alloyed Nb₃Sn, Physica B+C (Amsterdam) **135**, 359 (1985).

[26] R. Bormann, D.-Y. Yu, R. Hammond, T. Geballe, S. Foner, and E. McNiff, Origin of the B_{c2} enhancement in ternary Nb-Sn phases, IEEE Trans. Magn. **21**, 1140 (1985).

[27] H. Sekine, T. Takeuchi, and K. Tachikawa, Studies on the composite processed Nb-Hf/Cu-Sn-Ga high-field superconductors, IEEE Trans. Magn. **17**, 383 (1981).

[28] O. Horigami, T. Luhman, C. S. Pande, and M. Suenaga, Superconducting properties of $Nb_3(Sn_{1-x}Ga_x)$ by a solid-state diffusion process, Appl. Phys. Lett. **28**, 738 (1976).

[29] L. R. Motowidlo, P. J. Lee, C. Tarantini, S. Balachandran, A. K. Ghosh, and D. C. Larbalestier, An intermetallic powder-in-tube approach to increased flux-pinning in Nb_3Sn by internal oxidation of Zr, Supercond. Sci. Technol. **31**, 014002 (2018).

[30] X. Xu, J. Rochester, X. Peng, M. Sumption, and M. Tomsic, Ternary Nb_3Sn superconductors with artificial pinning centers and high upper critical fields, Supercond. Sci. Technol. **32**, 02LT01 (2019).

[31] M. B. Field, Youzhu Zhang, Hanping Miao, M. Gerace, and J. A. Parrell, Optimizing Nb_3Sn conductors for high field applications, IEEE Trans. Appl. Supercond. **24**, 6001105 (2014).

[32] S. Balachandran, C. Tarantini, P. J. Lee, F. Kametani, Y.-F. Su, B. Walker, W. L. Starch, and D. C. Larbalestier, Beneficial influence of Hf and Zr additions to Nb4at%Ta on the vortex pinning of Nb_3Sn with and without an O source, Supercond. Sci. Technol. **32**, 044006 (2019).

[33] N. Banno, T. Morita, T. Yagai, and S. Nimori, Influence of parent Nb-alloy grain morphology on the layer formation of Nb_3Sn and its flux pinning characteristics, Scr. Mater. **199**, 113822 (2021).

[34] C. Tarantini, F. Kametani, S. Balachandran, S. M. Heald, L. Wheatley, C. R. M. Grovenor, M. P. Moody, Y.-F. Su, P. J. Lee, and D. C. Larbalestier, Origin of the enhanced Nb_3Sn performance by combined Hf and Ta doping, Sci. Rep. **11**, 17845 (2021).

[35] N. R. Werthamer, E. Helfard, and P. C. Hohenberg, Temperature and purity dependence of the superconducting critical field, H_{c2}. III. Electron spin and spin-orbit effects, Phys. Rev. **147**, 295 (1966).

[36] H. Sekine, K. Tachikawa, and Y. Iwasa, Improvements of current-carrying capacities of the composite-processed Nb_3Sn in high magnetic fields, Appl. Phys. Lett. **35**, 472 (1979).

[37] S. Hong, J. Parrell, and M. Field, Method for producing $(Nb, Ti)_3Sn$ wire by use of Ti source rods, US Patent No. 6981309 (2004).

[38] J. A. Parrell, Youzhu Zhang, M. B. Field, P. Cisek, and Seung Hong, High field Nb_3Sn conductor development at Oxford Superconducting Technology, IEEE Trans. Appl. Supercond. **13**, 3470 (2003).

[39] C. Segal, C. Tarantini, Z. H. Sung, P. J. Lee, B. Sailer, M. Thoener, K. Schlenga, A. Ballarino, L. Bottura, B. Bordini, C. Scheuerlein, and D. C. Larbalestier, Evaluation of critical current density and residual resistance ratio limits in powder in tube Nb_3Sn conductors, Supercond. Sci. Technol. **29**, 085003 (2016).

[40] B. Bordini, L. Bottura, G. Mondonico, L. Oberli, D. Richter, B. Seeber, C. Senatore, E. Takala, and D. Valentinis, Extensive characterization of the 1 mm PIT Nb_3Sn strand for the 13-T FRESCA2 magnet, IEEE Trans. Appl. Supercond. **22**, 6000304 (2012).

[41] A. Ballarino *et al.*, The CERN FCC conductor development program: A worldwide effort for the future generation of high-field magnets, IEEE Trans. Appl. Supercond. **29**, 6000709 (2019).

[42] R. Flükiger, Martensitic transformations and their effects on superconductivity in A15 superconductors, J. Phys. Colloq. **43**, C4 (1982).

[43] R. Besson, S. Guyot, and A. Legris, Atomic-scale study of diffusion in A15 Nb_3Sn, Phys. Rev. B **75**, 054105 (2007).

[44] S. Balachandran, B. Walker, P. J. Lee, W. L. Starch, C. Tarantini, and D. C. Larbalestier, Comparative drawability and recrystallization evaluation of Nb4Ta and Nb4Ta1Hf alloys, and the beneficial influence of Hf on developing finer Nb_3Sn grain size, J. Alloys Compd. **984**, 173985 (2024).

[45] S. Balachandran, P. J. Lee, C. Tarantini, N. Paudel, C. B. Segal, M. Small, J. Tietsworth, W. L. Starch, and D. C. Larbalestier, Developments and progress in R&D Nb_3Sn wires made with commercial Nb4Ta1Hf alloy, presentation at the 2022 Applied Superconductivity Conference (2022).

[46] T. P. Orlando, E. J. McNiff, S. Foner, and M. R. Beasley, Critical fields, Pauli paramagnetic limiting, and material parameters of Nb_3Sn and V_3Si, Phys. Rev. B **19**, 4545 (1979).

[47] W. Goldacker, R. Ahrens, M. Nindel, B. Obst, and C. Meingast, HIP synthesized Nb_3Sn bulk materials with extraordinary homogeneity, IEEE Trans. Appl. Supercond. **3**, 1322 (1993).

[48] J. Zhou, Y. Jo, Z. Hawn Sung, H. Zhou, P. J. Lee, and D. C. Larbalestier, Evidence that the upper critical field of Nb_3Sn is independent of whether it is cubic or tetragonal, Appl. Phys. Lett. **99**, 122507 (2011).